MATERIALS CHEMISTRY FRONTIERS

RESEARCH ARTICLE

View Article Online
View Journal | View Issue

Cite this: *Mater. Chem. Front.*, 2021, **5**, 5351

A $CoSe_2$-based 3D conductive network for high-performance potassium storage: enhancing charge transportation by encapsulation and restriction strategy†

Jing Zhao,‡[a] Hu Wu,‡[a] Long Li,[a] Shiyao Lu,[b] Heng Mao[a] and Shujiang Ding *[a]

Potassium-ion batteries (PIBs) are expected as a supplement for lithium-ion batteries (LIBs) due to the abundant potassium resource and low cost. However, the large radius of the potassium ion hinders the ion transport dynamics and structural stability of the electrode material. Herein, a sandwich-like $CoSe_2$@NC/rGO composite is successfully synthesized by a two step co-precipitation and pyrolysis/selenization method. Taking full advantage of this unique 3D structure, the electronic conductivity of $CoSe_2$@NC/rGO-5 is about 20 times higher than that of $CoSe_2$@NC, and the specific surface area of $CoSe_2$@NC/rGO-5 is about 6 times higher than that of $CoSe_2$@NC, which provides sufficient reactive sites. Moreover, the empty space between graphene layers can effectively alleviate the volume expansion and prevent the peeling of the active material during cycling. As a consequence, the as-prepared $CoSe_2$@NC/rGO-5 anode exhibits high reversible capacity (527.5 mA h g^{-1} at 0.1 A g^{-1}), good cycle stability (226 mA h g^{-1} at 0.5 A g^{-1} after 400 cycles) and enhanced rate capability (206 and 157 mA h g^{-1} at 5 and 10 A g^{-1}, respectively). A two-step reaction process from $CoSe_2$ to K_2CoSe_2 to K_2Se during discharging is confirmed by *ex situ* TEM and *ex situ* XPS. This work provides a facile approach to prepare high-performance electrodes with a 3D conductive network, and further deepens the understanding of the evolution of $CoSe_2$ in the potassium storage process.

Received 5th March 2021,
Accepted 24th April 2021

DOI: 10.1039/d1qm00362c

rsc.li/frontiers-materials

Introduction

In recent years, lithium-ion batteries (LIBs) have been widely used in electronic products, electric vehicles, and large-scale energy storage systems due to the high power/energy density, low self-discharge, high voltage and long cycle life.[1–7] However, LIBs suffer from lithium resource shortage and high costs, restricting their application in the large-scale energy storage field.[8–11] Due to their abundant reserves and low price, sodium-ion batteries (SIBs) and PIBs have been widely considered by the academic community.[12–15] The standard electrode potential of PIBs (−2.93 V *vs.* SHE) is lower than that of SIBs (−2.71 V *vs.* SHE), indicating the higher working voltage and energy density.[16–19] In addition, the weak Lewis acidity and small Stokes radius (K: 3.6 Å; Na: 4.6 Å) of the potassium ion means higher ionic conductivity in organic electrolytes.[11,17] Therefore, PIBs are considered as a supplement for lithium-ion batteries for next generation energy storage systems.

However, the larger radius of the potassium ion will destroy the structure of host materials and limit the ion transport kinetics, which makes it a challenge to design high-performance anodes for PIBs.[16,20–23] Although commercial graphite can be used as the PIB anode, its low theoretical specific capacity (279 m A h g^{-1}) is not suitable for meeting the requirements of a commercial potassium ion battery anode.[8,24] And the metal oxide suffers from poor cycle stability and low specific capacity.[21,25,26] Alloying-type anodes have higher specific capacity, but the volume expansion is extremely serious (*e.g.*, ~681% for Sn_4P_3).[27] Chalcogenides have attracted extensive attention due to their high capacity, abundant resources and low price.[23,28–30] In particular, since the conductivity of selenium (1×10^{-3} S m^{-1}) is more than 20 orders of magnitude higher than that of sulfur (5×10^{-30} S m^{-1}), transition metal selenides are expected to be promising anodes for PIBs.[16] However, selenides confront a certain degree of volume change during the charging–discharging process. Reasonable structural design is an effective way to buffer the

[a] *School of Chemistry, Xi'an Key Laboratory of Sustainable Energy Materials Chemistry, State key laboratory of Electrical Insulation and Power Equipment, Department of Applied Chemistry, Xi'an Jiaotong University & Shaanxi Quantong Joint Research Institute of New Energy Vehicles Power, Xi'an Jiaotong University, Xi'an 710049, China. E-mail: dingsj@mail.xjtu.edu.cn*

[b] *Department of Chemistry, City University of Hong Kong, Hong Kong, China*

† Electronic supplementary information (ESI) available. See DOI: 10.1039/d1qm00362c

‡ J. Zhao and H. Wu contributed equally to this work.

volume change of the electrode material and improve its cycle stability. Li's group prepared VS_2 nanosheet assemblies with a few atomic layers thickness as a PIB anode, enabling the rapid and durable storage of K^+. The unique 3D hierarchical structure fully exposed their large surface areas and the open space between nanosheets and effectively buffered the volume change during repetitive cycling.[31] Lu's group successfully synthesized a spherical $MoSe_2$/N-doped carbon composite which still has a capacity of 258.02 mA h g^{-1} after 300 cycles at 100 mA g^{-1}, while the capacity of bare $MoSe_2$ begins to decay rapidly after 100 cycles.[32] Although these methods can solve some problems separately, a unique structural design with simple preparation and low energy consumption is what is most needed. And it is important that this structure can not only improve the electrical conductivity of the material, but also buffer the problem of poor circulation performance, resulting in volume changes, and improve the specific capacity of the electrode material.

Herein, we propose a novel and simple method for the preparation of a double carbon sandwich structure $CoSe_2$@NC/rGO-x (x = 0, 1, 5, and 10; the percentage by weight of GO) derived from a Metal–Organic Framework (MOF). In the sandwich structure, the N-doped carbon matrix (NC) from the pyrolysis of organic ligands is encapsulated by ultrafine $CoSe_2$ particles and combined with graphene to form a 3D conductive network. Benefiting from the unique structure, the as-prepared $CoSe_2$@NC/rGO-5 anode exhibits high reversible capacity (527.5 mA h g^{-1} at 0.1 A g^{-1}), good cycle stability (226 mA h g^{-1} at 0.5 A g^{-1} after 400 cycles) and high-rate capability. Even at a high current density of 10 A g^{-1}, a specific capacity of 175 mA h g^{-1} can be maintained. This excellent electrochemical performance is mainly attributed to the unique double carbon sandwich structure, which has the following advantages: (i) the 3D conductive network improves the electronic conductivity (4.6802×10^6 S cm^{-1} for $CoSe_2$@NC/rGO-5 and 2.3767×10^5 S cm^{-1} for $CoSe_2$@NC in Table S1, ESI†) and shortens the ion transport distance; (ii) the large specific surface area increases the reactive sites; (iii) the interspace between graphene layers can effectively alleviate the volume expansion and peeling of the material during cycling. Furthermore, a two-step reaction from $CoSe_2$ to K_2CoSe_2 to K_2Se during discharging is confirmed by *ex-situ* TEM/XPS, providing a deeper understanding of the evolution of $CoSe_2$ in the potassium storage process.

Results and discussion

A series of $CoSe_2$@NC/rGO-x nanocomposites were synthesized in this work, and the synthesis process of the sandwich structure $CoSe_2$@NC/rGO-x is schematically illustrated in Fig. 1, including two steps: (1) a co-precipitation method was employed to prepare the CoCoPBA@GO precursor; (2) through a relatively mild pyrolysis/selenization process, the sandwich-like $CoSe_2$@NC/rGO-x composite was obtained. The NC on the surface of $CoSe_2$ nanoparticles is generated by the pyrolysis of the organic components in CoCoPBA and interconnected with rGO to form a three-dimensional conductive network.

The morphology and microstructure of the samples were characterized using a scanning electron microscope (SEM) and high-resolution transmission electron microscope (TEM), as shown in Fig. 2. The regular cube with a uniform size (100–200 nm) and smooth surface of CoCoPBA is observed in Fig. 2b. After selenization in a tubular furnace, CoCoPBA cubes are converted to $CoSe_2$@NC with a rough surface (Fig. S2a, ESI†). Unfortunately, the regular cube structure is not maintained well and collapses into particles after selenization. In order to prevent the collapse and agglomeration of nanocubes and build a conductive network, we conducted a GO wrapping strategy to form a sandwich structure of CoCoPBA nanocubes evenly distributed on GO sheets (Fig. S1, ESI†). Most of the original cubic structure of CoCoPBA remains unchanged after selenization, indicating that rGO can effectively alleviate structural collapse during the heat treatment process (Fig. 2c and Fig. S2b, c, ESI†). The TEM images in Fig. 2d and e show that the $CoSe_2$@NC nanocubes are tightly wrapped by rGO sheets and the thickness of the NC layer is about 3.3 nm. The selected area electron diffraction (SAED) patterns in Fig. 2f present the (110), (211) and (311) diffraction rings of trogtalite $Pn\bar{3}$ space $CoSe_2$ and the (101), (120) and (211) diffraction rings of orthorhombic Pnnm space $CoSe_2$, confirming the successful formation of $CoSe_2$. The clear fringes with a spacing of 0.250 nm are consistent with the (120)

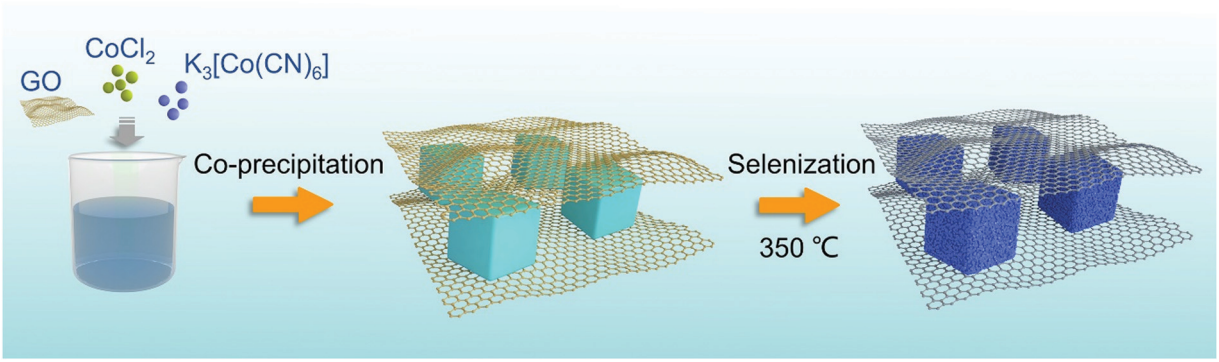

Fig. 1 Schematic of the synthesis process of $CoSe_2$@NC/rGO-x.

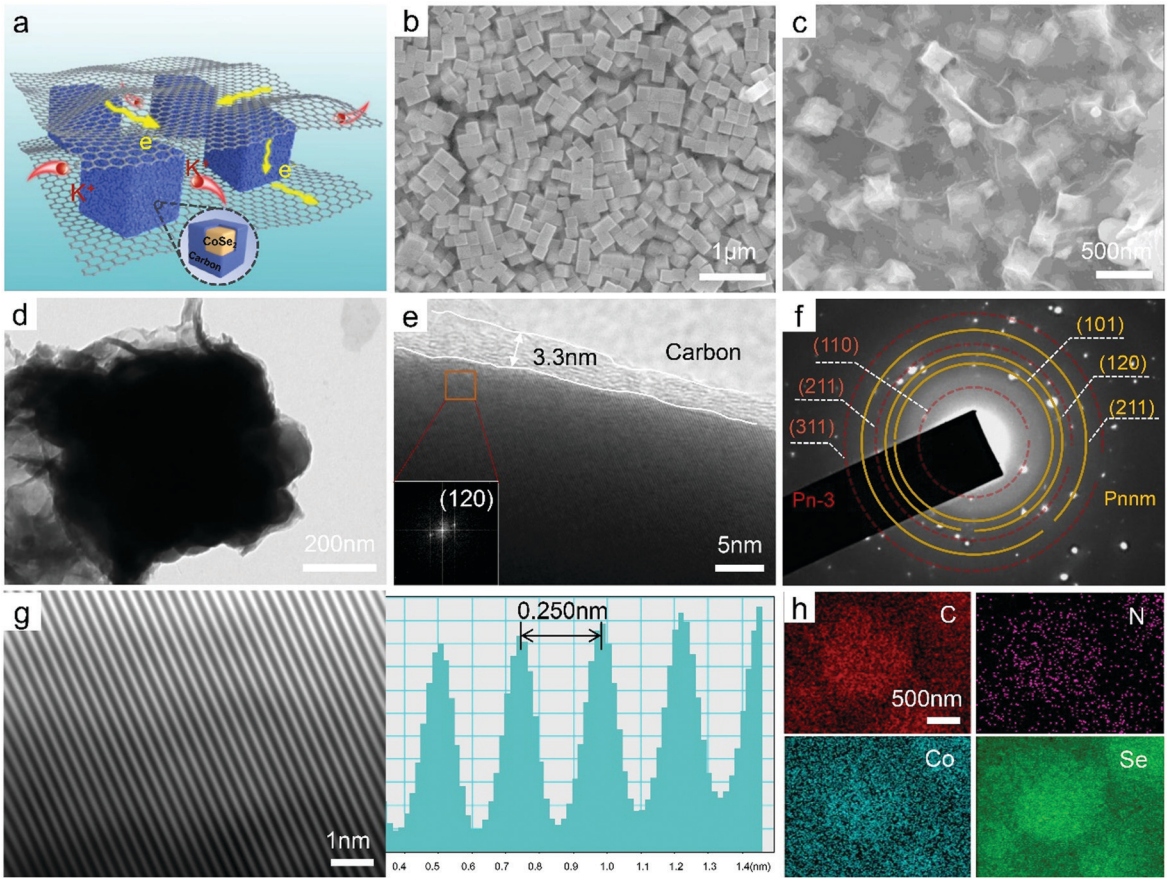

Fig. 2 (a) Schematic illustration of $CoSe_2$@NC/rGO-*x*. SEM images of (b) CoCoPBA and (c) $CoSe_2$@NC/rGO-5. (d) TEM image, (e and g) high-resolution TEM images and the corresponding interlayer spacing, (f) the SAED patterns and (h) element mapping of $CoSe_2$@NC/rGO-5.

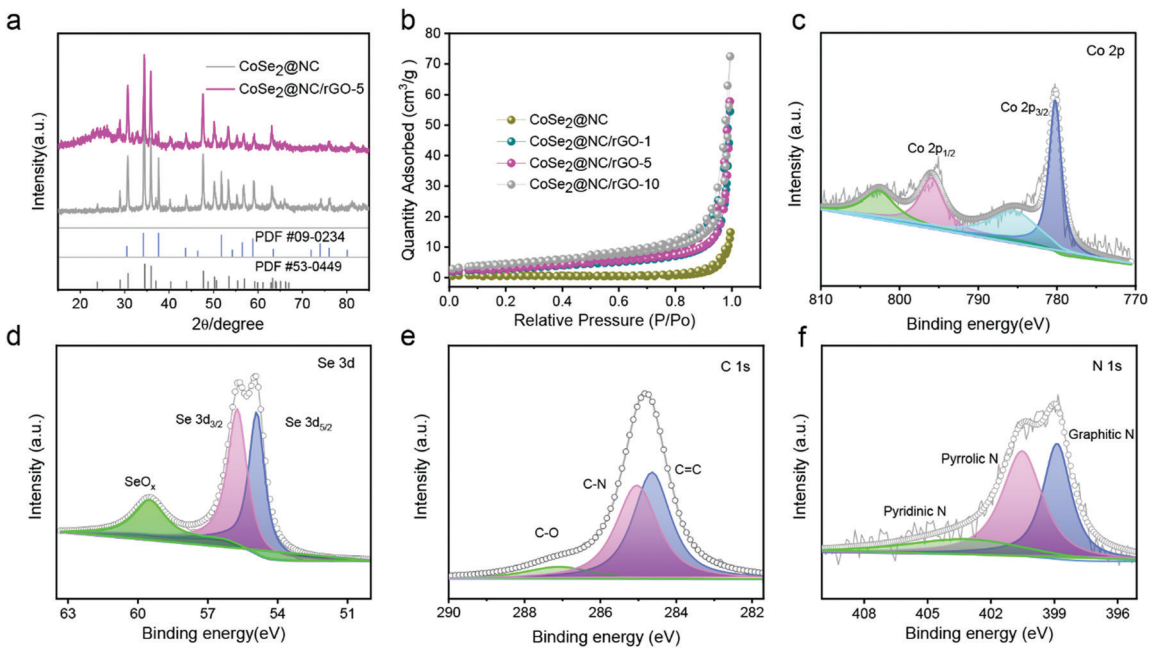

Fig. 3 (a) XRD patterns of $CoSe_2$@NC and $CoSe_2$@NC/rGO-5. (b) N_2 adsorption–desorption isotherms of $CoSe_2$@NC/rGO-*x*. XPS spectra of $CoSe_2$@NC/rGO-5: (c) Co 2p, (d) Se 3d, (e) C 1s and (f) N 1s.

crystal plane of orthorhombic phase $CoSe_2$ (Fig. 2g). The EDX elemental mapping images further reveal the uniform distribution of C, N, Co and Se elements in $CoSe_2$@NC/rGO-5 in Fig. 2h.

The X-ray diffraction (XRD) patterns of CoCoPBA and CoCoPBA@GO-5 are completely allocated to $Co_3(Co(CN)_6)_2$ (PDF # 22-0215) without any impurity peaks (Fig. S3, ESI†). As shown in Fig. 3a, the characteristic peak of CoCoPBA precursor disappears completely after selenization, which is replaced by the mixed crystal phase of trogtalite phase $CoSe_2$ ($Pn\bar{3}$, PDF # 09-0234) and orthorhombic phase $CoSe_2$ (Pnnm, PDF # 53-0449), consistent with the SAED results. With the addition of rGO, the observed broad peak at 26° can be attributed to the (002) facet of rGO.[33] When rGO was introduced into the samples, two strong characteristic peaks at 1346 cm^{-1} (D band) and 1585 cm^{-1} (G band) appear in Raman spectra (Fig. S4a, ESI†), which are attributed to the sp^3 and sp^2 vibration of hybridized carbons.[23,34] And the peaks at 188 cm^{-1} and 672 cm^{-1} are attributed to the A_{1g} and A_g modes of $CoSe_2$, while the three minor bands at 469, 511 and 607 cm^{-1} are possibly associated with the E_g, $F_{2g}^{(2)}$ modes and $F_{2g}^{(1)}$ modes of cobalt oxide caused by surface oxidation.[35] The nitrogen adsorption/desorption isotherm and pore size distribution are shown in Fig. 3b and Fig. S4b (ESI†). The specific surface areas of $CoSe_2$@NC, $CoSe_2$@NC/rGO-1, $CoSe_2$@NC/rGO-5 and $CoSe_2$@NC/rGO-10 are 2.2, 11.0, 13.0 and 16.6 $m^2\ g^{-1}$, respectively. Compared with $CoSe_2$@NC, $CoSe_2$@NC/rGO composites have a larger specific surface area and total pore volume. These results suggest that the introduction of rGO is conducive to the electrode reaction, thus accelerating ion diffusion, electron transfer and electrolyte penetration. In addition, the content of $CoSe_2$ in $CoSe_2$@NC, $CoSe_2$@NC/rGO-1, $CoSe_2$@NC/rGO-5 and $CoSe_2$@NC/rGO-10 is 98%, 92.3%, 86.9% and 57.8% by thermogravimetric analysis (TGA) (Fig. S5, ESI†).

The chemical composition and surface electronic states of the as-prepared $CoSe_2$@NC/rGO-5 were characterized by X-ray photoelectron spectroscopy (XPS) (Fig. 3c–f). The presence of oxygen can be attributed to the air adsorption on the sample surface or the COOH group on rGO, while the presence of N mainly comes from CoCoPBA.[36] From the high-resolution spectrum of Co 2p in Fig. 3c, two spin–orbit splitting peaks at 780.1 eV and 795.9 eV correspond to Co^{2+} $2p_{3/2}$ and Co^{2+} $2p_{1/2}$.[34] The peaks at 785.5 eV and 802.0 eV are attributed to the corresponding ''satellite peaks''(''Sat.'').[34] The high-resolution Se 3d spectrum in Fig. 3d shows three well-defined peaks at 55.7 eV, 54.9 eV and 59.5 eV, corresponding to the Se^- $3d_{3/2}$, Se^- $3d_{5/2}$ and SeO_x, respectively.[37,38] In the high-resolution spectrum of C 1s (Fig. 3e), three peaks at 284.6 eV, 285.1 eV and 287.2eV can be observed, which are attributed to C=C, C–N and C–O bonds, respectively.[20,39] However, the C 1s spectrum of $CoSe_2$@NC (Fig. S7, ESI†) does not exhibit the C–O signal, indicating no rGO in $CoSe_2$@NC. The N 1s spectrum of $CoSe_2$@NC/rGO-5 (Fig. 3f) shows the coexistence of graphite-N (398.4 eV), pyrrole-N (400.5 eV) and pyridine-N (403.8 eV).[40] The rich N-doping provides a large number of exogenous defects and active centers to improve the electron/ion transport in electrochemical reactions.

Driven by the three-dimensional interconnected conductive network between cubic particles and graphene sheets, $CoSe_2$@NC/rGO-x was assembled into the PIB as an anode material, and its electrochemical performance was evaluated using CR2025 coin-type cells. In order to fully demonstrate the material properties, 1 M KFSI in EC/DEC (v/v, 1 : 1) and CMC were selected as the appropriate electrolyte and binder by matching the composites as prepared with different electrolytes (0.8 M KPF_6 in EC/DEC (v/v, 1 : 1), 1 M KFSI in EC/DEC (v/v, 1 : 1) and 2 M KFSI in EC/DEC (v/v, 1 : 1)) and binders (PVDF and CMC), as shown in Fig. S8 (ESI†). Furthermore, by optimizing the amount of rGO, the electrochemical performance of the materials increased first and then decreased with the increase of graphene content (Fig. S9 (ESI†) and Fig. 4d).

In order to clarify the mechanism of potassium storage, we measured the cyclic voltammetry (CV) curves of the $CoSe_2$@NC/rGO-5 anode at a scan rate of 0.1 mV s^{-1}. As shown in Fig. 4a, three reduction peaks at 1.62, 0.71 and 0.35 V were observed in the first cathodic scan. At the weak peak of 1.62 V, K^+ is initially inserted into the $CoSe_2$@NC/rGO-5 electrode. The unique spike at 0.71 V can be attributed to the formation of the potassium insertion product (K_xCoSe_2) and the solid electrolyte interface (SEI) film. The peak at 0.35 V can be attributed to the full conversion reaction from K_xCoSe_2 to Co and K_2Se. In the first anodic scan, the two oxidation peaks observed at 1.87 V and 2.42 V are related to the regeneration of $CoSe_2$. In the next scans, CV curves almost coincide, indicating the excellent electrochemical reversibility of $CoSe_2$@NC/rGO-5. The charge–discharge curves at a current density of 100 mA g^{-1} of $CoSe_2$@NC/rGO-5 are shown in Fig. 4b. The voltage platform of the charge–discharge curve is consistent with the CV curves. The initial discharge capacity is 720 mA h g^{-1} with a high initial Coulombic efficiency (CE) of 72.6%. Only 27.4% of the irreversible capacity is lost, much lower than that of $CoSe_2$@NC (Fig. S9 (ESI†), 44.4% irreversible capacity loss). The generation of irreversible capacity is mainly caused by the formation of an SEI and the irreversible electrochemical processes.[41]

As we all know, cycling performance is crucial for rechargeable PIBs, due to the structural failure caused by repeated insertion/extraction of the large K^+. Fig. 4d compares the cycle stability of $CoSe_2$@NC and $CoSe_2$@NC/rGO-x at 100 mA g^{-1}. The electrode based on $CoSe_2$@NC delivers a capacity of 282.5 mA h g^{-1} in the third cycle, and maintains 236.4 mA h g^{-1} with 83.7% capacity retention after 100 cycles. The discharge capacity of $CoSe_2$@NC/rGO-1, $CoSe_2$@NC/rGO-5 and $CoSe_2$@NC/rGO-10 based PIBs in the third cycle is 328, 527 and 412 mA h g^{-1}, respectively. After 100 cycles, the remaining capacity is 308, 521 and 336 mA h g^{-1}, respectively, and capacity retention rates are 93.3%, 98.8% and 81.5%. Obviously, the $CoSe_2$@NC/rGO-5 electrode has the highest specific capacity and capacity retention rate, due to the synergistic effect of $CoSe_2$@NC and rGO. In addition, $CoSe_2$@NC/rGO-5 exhibits a reversible capacity of 226 mA h g^{-1} at 0.5 A g^{-1} after 400 cycles (Fig. 4e). However, the capacity of $CoSe_2$@NC decays to tens after 200 cycles at a current density of 0.5 A g^{-1}. Therefore, it is speculated that there may be serious structural aberrations in the process of potassiation/depotassiation of $CoSe_2$. The sandwich

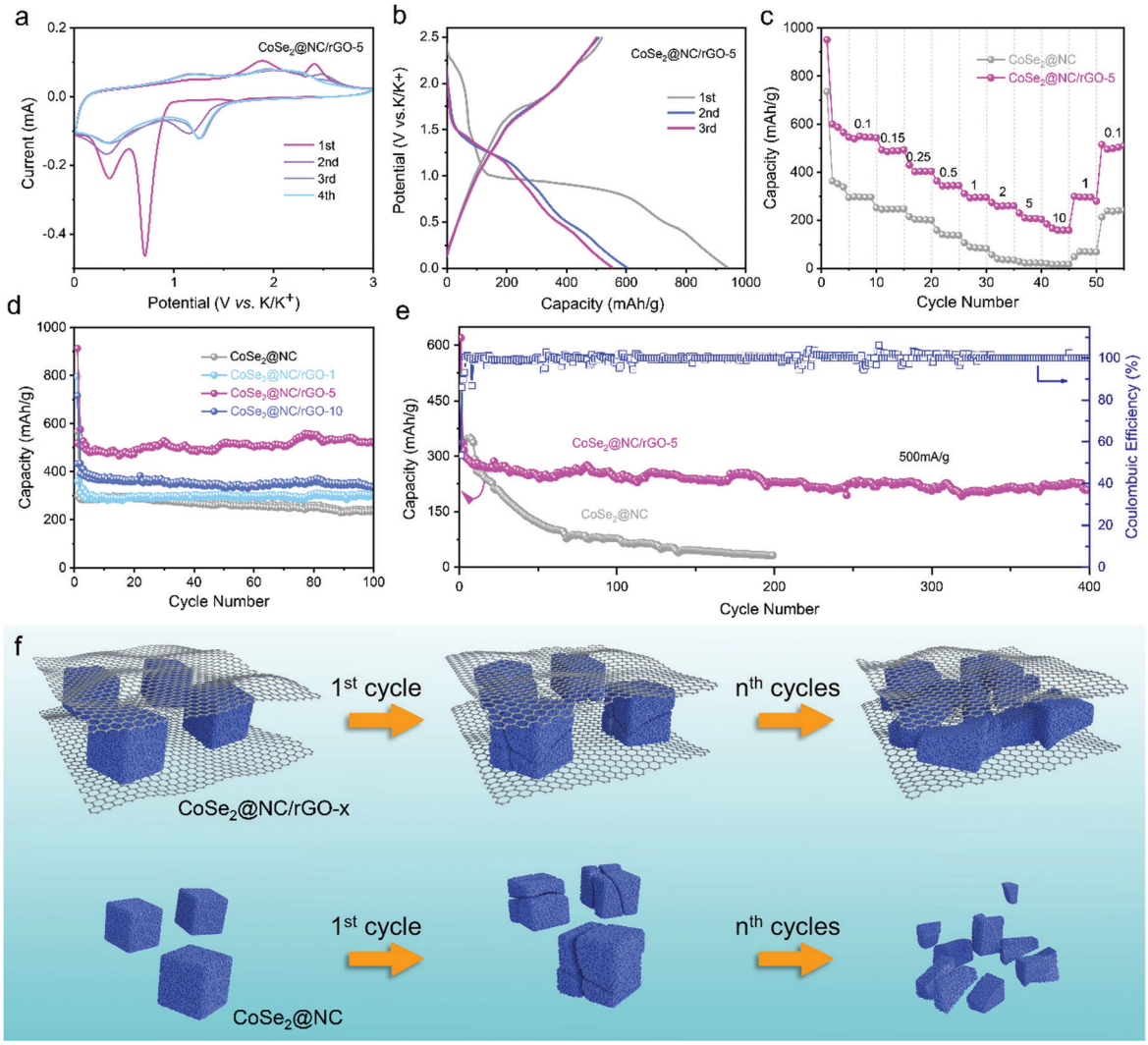

Fig. 4 (a) The CV curves of the first several cycles of $CoSe_2$@NC/rGO-5 electrode at a scan rate of 0.1 mV s^{-1}. (b) Charge/discharge profiles of $CoSe_2$@NC/rGO-5 electrode for the first three cycles. (c) Rate performance of $CoSe_2$@NC and $CoSe_2$@NC/rGO-5 at various current densities from 0.1 to 2 A g^{-1}. (d) Cycling performance of $CoSe_2$@NC and $CoSe_2$@NC/rGO-*x* electrodes at a current density of 0.1 A g^{-1}. (e) Long-term cycling performance of $CoSe_2$@NC and $CoSe_2$@NC/rGO-5 electrodes at the current density of 0.5 A g^{-1}. (f) Schematic diagram of $CoSe_2$@NC and $CoSe_2$@NC/rGO-5 after *n*th cycles.

structure of $CoSe_2$@NC/rGO-5 is beneficial to prevent $CoSe_2$ particles from detaching from the electrode for the volume change during cycling (Fig. 4f and Fig. S13, ESI†). From the SEM images of $CoSe_2$@NC and $CoSe_2$@NC/rGO-5 electrodes after 50 cycles, it was found that the cubes of the $CoSe_2$@NC electrode had basically scattered into small particles after charging and discharging processes. The poor contact between conductive carbon black and crushed active material leads to the serious capacity loss of $CoSe_2$@NC. For $CoSe_2$@NC/rGO-5, the cubes are coated by graphene and retain the bulk, resulting in good electronic contact with the collector and good cycle stability. Moreover, compared with other reported transition metal compounds (Table S2, ESI†), $CoSe_2$@NC/rGO-5 shows higher specific capacity and cycle stability. This is mainly caused by the special three-dimensional conductive structure with a large space and multiple microchannels, which effectively buffers volume changes and improves charge transfer. Therefore, this structural optimization leads to the increase of capacity and stability.

Electrochemical impedance spectroscopy (EIS) at the open circuit voltage (OCV) of $CoSe_2$@NC/rGO-5 and $CoSe_2$@NC electrodes was performed (Fig. S10, ESI†). In Nyquist plots, the intercept of the high frequency region and the real axis, the semicircle of the high frequency region and the diagonal line of the low frequency region correspond to the internal resistance (R_s), the interface charge transfer resistance (R_{ct}) and the Warburg resistance related to K^+ diffusion, respectively. The R_s and R_{ct} of $CoSe_2$@NC/rGO-*x* electrodes are smaller than those of $CoSe_2$@NC electrodes. The $CoSe_2$@NC/rGO-5 electrode exhibits the smallest R_{ct} value, which can be attributed to the improved conductivity of the 3D network and the enhanced charge transfer kinetics enabled by the rich reactive sites. Besides, from the EIS curve of cycled electrodes (Fig. S10b,

ESI†), it can be seen that the semicircle diameter of the electrode in the high frequency field decreases after 50 cycles, which indicates that the charge transfer in the electrode becomes faster and its ion/electron conductivity increases rapidly after cycling. The minimum semicircle of the $CoSe_2$@NC/rGO-5 anode at high frequency indicates that the ion/electron conductivity of the electrode is the highest.

The rate performance of $CoSe_2$@NC and $CoSe_2$@NC/rGO-5 is shown in Fig. 4c. $CoSe_2$@NC/rGO-5 shows excellent rate performance in the range of 0.1 to 10 A g^{-1}, providing reversible specific capacities of 543, 476, 408, 339, 294, 259, 206 and 157 mA h g^{-1} at 0.1, 0.15, 0.25, 0.5, 1, 2, 5 and 10 A g^{-1}. When the current density returns to 0.1 A g^{-1}, the capacity of the battery shows almost no decline compared to the original, showing impressive reversibility. The excellent rate performance can be observed more clearly in charge–discharge curves under different current densities (Fig. S11, ESI†).

CV tests were carried out at different scanning speeds (0.2–1.0 mV s^{-1}) to understand the better rate performance of the $CoSe_2$@NC/rGO-5 electrode, and the curves show similar shapes at different scan rates, as shown in Fig. 5.

In general, the scanning rate (v) and the test current (i) are subject to the following relationship:

$$i = av^b \quad (1)$$

By simply transforming this eqn

$$\log i = b\cdot\log v + \log a \quad (2)$$

where both a and b are adjustable parameters and the value of b is the slope of the linear relationship between $\log i$ and $\log v$, and its magnitude can represent the K^+ storage mechanism. b = 0.5 stands for that the electrode reaction is K^+ embedding/stripping reaction, that is, diffusion process. b = 1 stands for that the electrode reaction is a capacitive behavior, which is controlled by the surface reaction and represents the capacitive controlled process.

The slope b value of the redox peak calculated by the log$i$ - log$v$ relationship in Fig. 5b is 0.72 (peak 1), 0.84 (peak 2) and 0.91 (peak 3) respectively, indicating that the kinetic process of the electrode is mainly a capacitive controlled process. In addition, the relative contributions from capacitive behavior (k_1v) and diffusion behavior ($k_2v^{1/2}$) at a fixed potential can be obtained by the following equation:

$$i = k_1v + k_2v^{1/2} \quad (3)$$

By calculating the value of k_1, the specific proportion of capacitor storage in the whole electrochemical process can be determined. According to the aforementioned method, when the sweep is 0.8 mV s^{-1}, the contribution of the electrode capacitance controlled process is 66% (Fig. 5c). Fig. 6d summarizes the contribution of the capacitive behavior at different scan rates. When the scan rate was 0.2, 0.4, 0.6, 0.8 and 1.0 mV s^{-1}, the corresponding contribution rates were 51%, 56%, 61%, 66% and 71%, respectively. The results show that the electrochemical process in the electrode is the coexistence

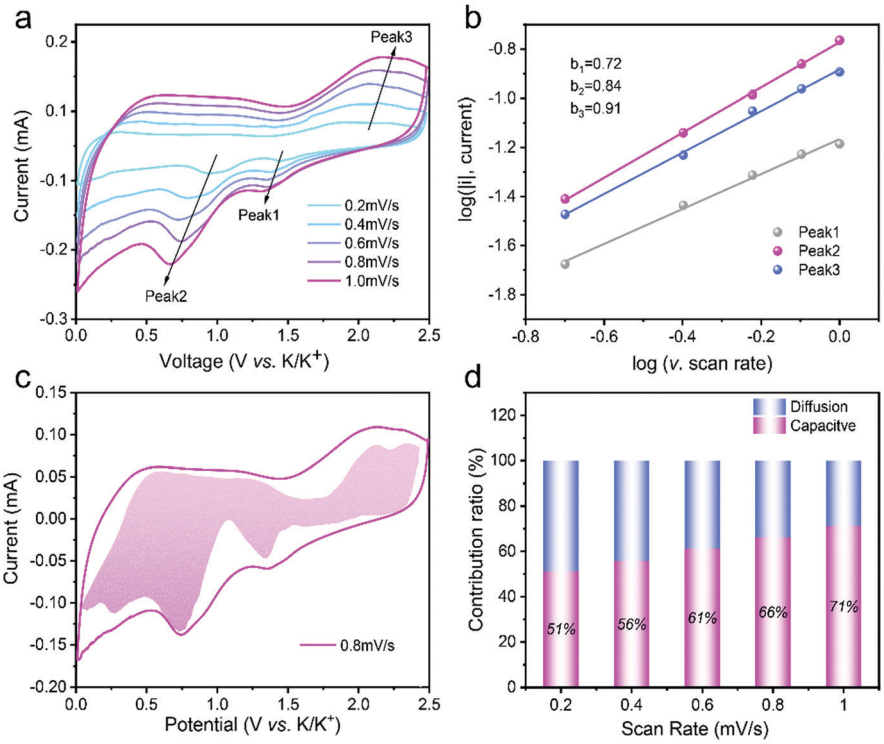

Fig. 5 (a) The CV curves of the $CoSe_2$@NC/rGO-5 electrode at various scan rates. (b) Determination of the b values using the relationship between peak current and scan rate. (c) Separation of the capacitive current in the $CoSe_2$@NC/rGO-5 electrode at a scan rate of 0.8 mV s^{-1} with the capacitive fraction shown by the shaded region. (d) Relative contribution of the capacitive and diffusion-controlled charge storage at different scan rates.

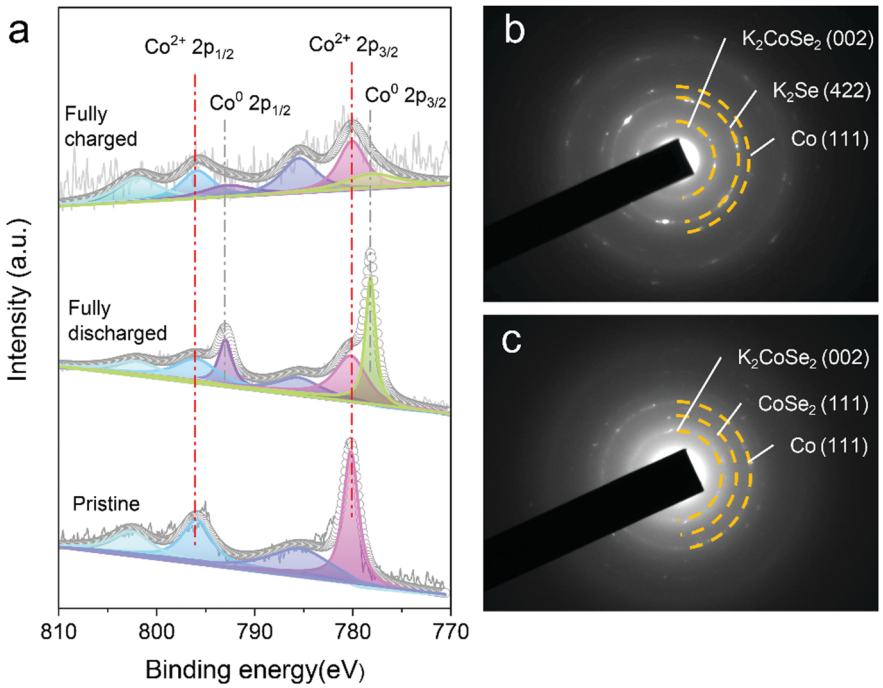

Fig. 6 *Ex situ* XPS data of (a) Co 2p peaks for pristine, fully discharged and fully charged $CoSe_2$@NC/rGO-5. (b and c) HRTEM images of the fully discharged, fully charged $CoSe_2$@NC/rGO-5 electrodes after 5 cycles.

of capacitive storage and diffusion processes, but the capacitive behavior is dominant. Compared with the pseudocapacitive behavior of $CoSe_2$@NC (Fig. S12, ESI†), the contribution ratios of $CoSe_2$@NC/rGO-*x* were larger. This result further proves that *in situ* NC coating and rGO wrapping can optimize the surface reaction and achieve fast electron/ion transport dynamics, leading to the enhanced pseudocapacitive energy storage.

In order to further comprehend the mechanism of $CoSe_2$ to store K^+, *ex situ* XPS and TEM were conducted to analyze the $CoSe_2$ with different potentials. Fig. 6a shows the Co 2p XPS spectra of the $CoSe_2$@NC/rGO-5 electrode in the original, fully discharged and charged state. For the original $CoSe_2$@NC/rGO-5 electrode, there are two main peaks in the XPS spectrum at 780.1 and 795.9 eV, corresponding to the $2p_{3/2}$ and $2p_{1/2}$ binding energies of Co^{2+} in $CoSe_2$, respectively.[34] Other peaks at 785.5 and 802.0 eV are attributed to the corresponding satellite peaks ("Sat.").[34] Two new peaks at 777.7 and 792.8 eV were observed, corresponding to Co^0 $2p_{3/2}$ and $2p_{1/2}$.[42] This indicates that K_xCoSe_2 and Co^0 are the results of potassium ion insertion. When the electrode is full of 2.5 V, the peak of Co^{2+} shifts back to the position of high binding energy similar to the original state due to the release of potassium ions from K_xCoSe_2 to $CoSe_2$. The relative strength of the 782.8 eV peak decreases but does not disappear, suggesting that the charge reaction does not complete. For the Se 3d peak, when the electrode is discharged to 0.01 V and then charged to 2.5 V, the peak shifts to lower binding energy and then to higher binding energy, indicating the reduction process from Se^- to Se^{2-} and the oxidation process from Se^{2-} to Se^- (Fig. S13a, ESI†). This result is consistent with the trend of the Co^{2+} peak. Fig. 6b, c and Fig. S13b, c (ESI†) show the *ex situ* HRTEM images and corresponding SAED patterns with five cycles of full discharge and full charge of the $CoSe_2$@NC/rGO-5 electrode. When the electrode is fully discharged to 0.01 V, the HRTEM images show clear lattice stripes with the crystal plane spacing of 0.685 nm and 0.295 nm, which are well matched with the K_2CoSe_2 (002) and K_2Se (220) crystal planes, respectively (Fig. S13b, ESI†). The corresponding diffraction patterns show a K_2CoSe_2 (002) diffraction ring, Co (111) diffraction ring and K_2Se (422) diffraction ring. When the electrode is fully discharged to 2.5 V, clear lattice fringes of the K_2CoSe_2 (002) and $CoSe_2$ (120) crystal planes are observed in Fig. S13c (ESI†), with the spacing of 0.685 nm and 0.250 nm, respectively. At the same time, a K_2CoSe_2 (002) diffraction ring, $CoSe_2$ (111) diffraction ring and Co (111) diffraction ring were detected in the diffraction pattern (Fig. 6c). Therefore, according to CV, XPS and TEM results, the reaction mechanism of $CoSe_2$ can be proposed as follows:

$$CoSe_2 + 2K^+ + 2e^- \leftrightarrow K_2CoSe_2 \quad (4)$$

$$K_2CoSe_2 + 2K^+ + 2e^- \leftrightarrow 2K_2Se + Co \quad (5)$$

Experimental

Preparation of the CoCoPBA microcubes

CoCoPBA microcubes were synthesized by a simple coprecipitation method using cobalt chloride and potassium hexacyanocobaltate as the cobalt source. In a typical synthesis, 3 mmol cobalt chloride and 4.5 mmol citric acid were dissolved in 200 mL deionized water to obtain clear pink solution A. Transparent solution B was obtained by dissolving 2 mmol potassium hexacyanocobaltate in 200 mL deionized water. B was added to A drop by drop under

magnetic stirring, and the mixed solution was stirred vigorously for 30 min and aged for 24 h at room temperature, followed by centrifugation and washing with deionized water and ethanol several times to collect the precipitates.

Preparation of the CoCoPBA/graphene composites

First, the graphene oxide was prepared by the classical Hummers' method. Then different concentrations of graphene oxide aqueous solutions (0.03 mg mL^{-1}, 0.15 mg mL^{-1} and 0.3 mg mL^{-1}) were prepared. 4.5 mmol citric acid and 3 mmol cobalt chloride were dissolved in 200 mL GO solution and stirred for 2 h to obtain the solution A. 2 mmol potassium hexacyanocobaltate were dissolved in 200 mL deionized water to form a transparent solution B. Then the solution B was added to the A drop by drop under magnetic agitation, stirred vigorously for 30 min, and then aged for 24 h at room temperature. The precipitate was washed several times with deionized water and freeze-dried for 24 h to obtain CoCoPBA/GO. The samples were labeled as CoCoPBA/GO-1, CoCoPBA/GO-5, and CoCoPBA/GO-10 according to the ratio of GO at 1%, 5% and 10%, respectively.

Preparation of the $CoSe_2$@NC/rGO-*x* composites

The obtained pink CoCoPBA powder or black CoCoPBA@GO powder was placed at one end of the porcelain boat, and the other side was placed with three times as much quality of selenium powder. The porcelain boat was transferred to a tube furnace with selenium powder in the upstream. The samples were heated at 350 °C for 5 h with a ramping rate of 2 °C/min under a 10% Ar/H_2 atmosphere. Then $CoSe_2$ composite materials were obtained and marked as $CoSe_2$@NC, $CoSe_2$@NC/rGO-1, $CoSe_2$@NC/rGO-5, and $CoSe_2$@NC/rGO-10, respectively.

Materials characterization

The morphologies and microstructure of the $CoSe_2$ composite materials were characterized by field emission scanning electron microscopy (SEM, JSM-7000F) and high-resolution transmission electron microscopy (TEM, JEM-2100, 200 kV). The X-ray diffraction (XRD) profile (Bruker D8 Advance Diffractometer with Cu target and Kα radiation) was collected over the 2θ range of 10–80° at 0.02° to characterize the crystal structure of the $CoSe_2$ composite materials. The valence states of the $CoSe_2$ composite materials were identified by X-ray photoelectron spectroscopy (XPS, Thermo Fisher ESCALAB Xi+). In addition, Raman spectroscopy was performed using a Raman microscope (hr800) with 514.5 nm laser excitation. The N_2 adsorption–desorption isotherms were measured and the specific surface areas and the pore size distributions were calculated based on the Brunauer–Emmett–Teller (BET) and the Barrett–Joyner–Halenda (BJH) models, respectively. Thermogravimetric analysis (TGA2, Mettler-Toledo) was employed to analyze the weight percentages of carbon in $CoSe_2$ composite materials under air over a temperature range of 30–800 °C with a ramping rate of 10 °C min^{-1}.

Electrochemical measurements

A CR2025 coin-type cell was used for electrochemical characterization. The active material : Super-p : CMC in a ratio of 7 : 2 : 1 was mixed into a slurry and coated on copper foil. The working electrode was obtained by vacuum drying at 60 °C for 12 h and punched into a disc with a diameter of 1.2 cm; the loading capacity of the active material is about 1.0 mg cm^{-2}. Potassium ion batteries were assembled in a glove box filled with high purity argon by using 1 M KFSI in EC/DEC (v/v, 1 : 1) as the electrolyte, a GF/D glass microfiber as the separator and a thin potassium sheet as the anode.

The galvanostatic discharge/charge tests of the batteries were conducted on a NEWARE Cycler CT-4000 (NEWARE Electronic Co., Shenzhen, China) battery measurement system at 0.01–2.5 V *versus* K^+/K. A CHI660E electrochemical workstation was employed for cyclic voltammetry (CV) and electrochemical impedance spectroscopy (EIS).

Conclusions

In this work, a sandwich-like $CoSe_2$@NC/rGO composite derived from a MOF was successfully synthesized by a two step co-precipitation and pyrolysis/selenization method. The unique structure creates a 3D conductive network and increases the specific surface area of the electrode, thus increasing the electrical conductivity and reactive sites. Meanwhile, rGO wrapping is beneficial to ease the volume expansion during cycling. Therefore, PIBs with the $CoSe_2$@NC/rGO-5 anode deliver high specific capacity, good cycle stability and high-rate capability. Even at a high current density of 10 A g^{-1}, a high specific capacity of 175 mA h g^{-1} can be maintained. Furthermore, *ex situ* TEM/XPS confirmed that $CoSe_2$ goes through a two-step reaction during discharging. Thus, this work provides an in-depth understanding of the evolution of potassium $CoSe_2$ storage processes, while also providing ideas for the rational design of other high-performance materials.

Author contributions

Jing Zhao: conceptualization, data curation, formal analysis, investigation, methodology, project administration, writing – original draft, and writing – review & editing; Hu Wu: project administration, data curation, validation, and writing – review & editing; Long Li: data curation and writing – review & editing; Shiyao Lu: investigation and methodology; Heng Mao: writing – review & editing; Shujiang Ding: supervision, resources, writing – review &, editing, and funding acquisition.

Conflicts of interest

There are no conflicts to declare.

Acknowledgements

This research was supported by the National Natural Science Foundation of China (No. 51773165), Key Laboratory Construction Program of Xi'an Municipal Bureau of Science and Technology (201805056ZD7CG40), Innovation Capability Support Program of

Shaanxi (No. 2018PT-28 and 2019PT-05), and the Natural Science Foundation of Shaanxi Province (2020JQ-018). The authors thank Mr Ren Zijun of Instrument Analysis and Testing Center of Xi'an Jiaotong University for his help with SEM and Mr Huang Chang for his help with XRD. The authors would like to thank the Center for Advancing Materials Performance from the Nanoscale (CAMP-Nano) for allowing the use of field-emission scanning electron microscopy.

References

1 J. Liao, Q. Hu, J. Mu, X. He, S. Wang, D. Jiemin and C. Chen, In situ carbon coated flower-like VPO_4 as an anode material for potassium-ion batteries, *Chem. Commun.*, 2019, **55**, 13916–13919.

2 G. Zheng, Y. Xiang, L. Xu, H. Luo, B. Wang, Y. Liu, X. Han, W. Zhao, S. Chen, H. Chen, Q. Zhang, T. Zhu and Y. Yang, Controlling Surface Oxides in Si/C Nanocomposite Anodes for High-Performance Li-Ion Batteries, *Adv. Energy Mater.*, 2018, **8**, 1801718.

3 C. Tang, Y. Liu, C. Xu, J. Zhu, X. Wei, L. Zhou, L. He, W. Yang and L. Mai, Ultrafine Nickel-Nanoparticle-Enabled SiO_2 Hierarchical Hollow Spheres for High-Performance Lithium Storage, *Adv. Funct. Mater.*, 2018, **28**, 1704561.

4 N. Wang, C. Chu, X. Xu, Y. Du, J. Yang, Z. Bai and S. Dou, Comprehensive New Insights and Perspectives into Ti-Based Anodes for Next-Generation Alkaline Metal (Na^+, K^+) Ion Batteries, *Adv. Energy Mater.*, 2018, **8**, 1801888.

5 J. Qian, C. Wu, Y. Cao, Z. Ma, Y. Huang, X. Ai and H. Yang, Prussian Blue Cathode Materials for Sodium-Ion Batteries and Other Ion Batteries, *Adv. Energy Mater.*, 2018, **8**, 1702619.

6 Y. Zhou, D. Yan, H. Xu, J. Feng, X. Jiang, J. Yue, J. Yang and Y. Qian, Hollow nanospheres of mesoporous Co_9S_8 as a high-capacity and long-life anode for advanced lithium ion batteries, *Nano Energy*, 2015, **12**, 528–537.

7 Y. Zhou, M. Zhang, Q. Wang, J. Yang, X. Luo, Y. Li, R. Du, X. Yan, X. Sun, C. Dong, X. Zhang and F. Jiang, Pseudocapacitance boosted N-doped carbon coated Fe_7S_8 nanoaggregates as promising anode materials for lithium and sodium storage, *Nano Res.*, 2020, **13**, 691–700.

8 Y. An, H. Fei, G. Zeng, L. Ci, B. Xi, S. Xiong and J. Feng, Commercial expanded graphite as a low–cost, long-cycling life anode for potassium–ion batteries with conventional carbonate electrolyte, *J. Power Sources*, 2018, **378**, 66–72.

9 Z. Liu, P. Li, G. Suo, S. Gong, W. Wang, C.-Y. Lao, Y. Xie, H. Guo, Q. Yu, W. Zhao, K. Han, Q. Wang, M. Qin, K. Xi and X. Qu, Zero-strain $K_{0.6}Mn_1F_{2.7}$ hollow nanocubes for ultra-stable potassium ion storage, *Energy Environ. Sci.*, 2018, **11**, 3033–3042.

10 M. Morant-Giner, R. Sanchis-Gual, J. Romero, A. Alberola, L. García-Cruz, S. Agouram, M. Galbiati, N. M. Padial, J. C. Waerenborgh, C. Martí-Gastaldo, S. Tatay, A. Forment-Aliaga and E. Coronado, Prussian Blue@MoS_2 Layer Composites as Highly Efficient Cathodes for Sodium- and Potassium-Ion Batteries, *Adv. Funct. Mater.*, 2018, **28**, 1706125.

11 H. Kim, J. C. Kim, M. Bianchini, D.-H. Seo, J. Rodriguez-Garcia and G. Ceder, Recent Progress and Perspective in Electrode Materials for K-Ion Batteries, *Adv. Energy Mater.*, 2018, **8**, 1702384.

12 B. Ji, F. Zhang, X. Song and Y. Tang, A Novel Potassium-Ion-Based Dual-Ion Battery, *Adv. Mater.*, 2017, **29**, 1700519.

13 A. Eftekhari, Z. Jian and X. Ji, Potassium Secondary Batteries, *ACS Appl. Mater. Interfaces*, 2017, **9**, 4404–4419.

14 Y. Fang, X. Y. Yu and X. W. D. Lou, Formation of Hierarchical Cu-Doped $CoSe_2$ Microboxes *via* Sequential Ion Exchange for High-Performance Sodium-Ion Batteries, *Adv. Mater.*, 2018, **30**, 1706668.

15 C. Jiang, Y. Fang, W. Zhang, X. Song, J. Lang, L. Shi and Y. Tang, A Multi-Ion Strategy towards Rechargeable Sodium-Ion Full Batteries with High Working Voltage and Rate Capability, *Angew. Chem., Int. Ed.*, 2018, **57**, 16370–16374.

16 Y. Yao, M. Chen, R. Xu, S. Zeng, H. Yang, S. Ye, F. Liu, X. Wu and Y. Yu, CNT Interwoven Nitrogen and Oxygen Dual-Doped Porous Carbon Nanosheets as Free-Standing Electrodes for High-Performance Na–Se and K–Se Flexible Batteries, *Adv. Mater.*, 2018, **30**, 1805234.

17 X. Niu, Y. Zhang, L. Tan, Z. Yang, J. Yang, T. Liu, L. Zeng, Y. Zhu and L. Guo, Amorphous $FeVO_4$ as a promising anode material for potassium-ion batteries, *Energy Storage Mater.*, 2019, **22**, 160–167.

18 C. Shen, K. Yuan, T. Tian, M. Bai, J. G. Wang, X. Li, K. Xie, Q. G. Fu and B. Wei, Flexible Sub-Micro Carbon Fiber@CNTs as Anodes for Potassium-Ion Batteries, *ACS Appl. Mater. Interfaces*, 2019, **11**, 5015–5021.

19 Y. H. Zhu, Y. B. Yin, X. Yang, T. Sun, S. Wang, Y. S. Jiang, J. M. Yan and X. B. Zhang, Transformation of Rusty Stainless-Steel Meshes into Stable, Low-Cost, and Binder-Free Cathodes for High-Performance Potassium-Ion Batteries, *Angew. Chem., Int. Ed.*, 2017, **56**, 7881–7885.

20 Y. Li, W. Zhong, C. Yang, F. Zheng, Q. Pan, Y. Liu, G. Wang, X. Xiong and M. Liu, N/S codoped carbon microboxes with expanded interlayer distance toward excellent potassium storage, *Chem. Eng. J.*, 2019, **358**, 1147–1154.

21 H. Qiu, L. Zhao, M. Asif, X. Huang, T. Tang, W. Li, T. Zhang, T. Shen and Y. Hou, SnO_2 nanoparticles anchored on carbon foam as a freestanding anode for high performance potassium-ion batteries, *Energy Environ. Sci.*, 2020, **13**, 571–578.

22 H. Lin, M. Li, X. Yang, D. Yu, Y. Zeng, C. Wang, G. Chen and F. Du, Nanosheets-Assembled CuSe Crystal Pillar as a Stable and High-Power Anode for Sodium-Ion and Potassium-Ion Batteries, *Adv. Energy Mater.*, 2019, **9**, 1900323.

23 J. Xie, Y. Zhu, N. Zhuang, H. Lei, W. Zhu, Y. Fu, M. S. Javed, J. Li and W. Mai, Rational design of metal organic framework-derived FeS_2 hollow nanocages@reduced graphene oxide for K-ion storage, *Nanoscale*, 2018, **10**, 17092–17098.

24 Z. Jian, W. Luo and X. Ji, Carbon Electrodes for K-Ion Batteries, *J. Am. Chem. Soc.*, 2015, **137**, 11566–11569.

25 G. Suo, D. Li, L. Feng, X. Hou, Y. Yang and W. Wang, SnO_2 nanosheets grown on stainless steel mesh as a binder free anode for potassium ion batteries, *J. Electroanal. Chem.*, 2019, **833**, 113–118.

26 C. Liu, S. Luo, H. Huang, Y. Zhai and Z. Wang, Direct Growth of MoO_2/Reduced Graphene Oxide Hollow Sphere Composites as Advanced Anode Materials for Potassium-Ion Batteries, *ChemSusChem*, 2019, **12**, 873–880.

27 Y. L. Wenchao Zhang and Z. Guo, Approaching high-performance potassium-ion batteries *via* advanced design strategies and engineering, *Sci. Adv.*, 2019, **5**, eaav7412.

28 D.-S. Bin, S.-Y. Duan, X.-J. Lin, L. Liu, Y. Liu, Y.-S. Xu, Y.-G. Sun, X.-S. Tao, A.-M. Cao and L.-J. Wan, Structural engineering of SnS_2/Graphene nanocomposite for high-performance K-ion battery anode, *Nano Energy*, 2019, **60**, 912–918.

29 L. Wang, J. Zou, S. Chen, G. Zhou, J. Bai, P. Gao, Y. Wang, X. Yu, J. Li, Y.-S. Hu and H. Li, TiS_2 as a high performance potassium ion battery cathode in ether-based electrolyte, *Energy Storage Mater.*, 2018, **12**, 216–222.

30 H. Yu, X. Cheng, M. Xia, T. Liu, W. Ye, R. Zheng, N. Long, M. Shui and J. Shu, Pretreated commercial $TiSe_2$ as an insertion-type potassium container for constructing ''Rocking-Chair'' type potassium ion batteries, *Energy Storage Mater.*, 2019, **22**, 154–159.

31 J. Zhou, L. Wang, M. Yang, J. Wu, F. Chen, W. Huang, N. Han, H. Ye, F. Zhao, Y. Li and Y. Li, Hierarchical VS_2 Nanosheet Assemblies: A Universal Host Material for the Reversible Storage of Alkali Metal Ions, *Adv. Mater.*, 2017, **29**, 1702061.

32 J. Ge, L. Fan, J. Wang, Q. Zhang, Z. Liu, E. Zhang, Q. Liu, X. Yu and B. Lu, $MoSe_2$/N-Doped Carbon as Anodes for Potassium-Ion Batteries, *Adv. Energy Mater.*, 2018, **8**, 1801477.

33 J. Li, X. Liu, L. Pan, W. Qin, T. Chen and Z. Sun, MoS_2–reduced graphene oxide composites synthesized via a microwave-assisted method for visible-light photocatalytic degradation of methylene blue, *RSC Adv.*, 2014, **4**, 9647.

34 Y. Huang, Z. Wang, Y. Jiang, S. Li, Z. Li, H. Zhang, F. Wu, M. Xie, L. Li and R. Chen, Hierarchical porous $Co_{0.85}Se$@reduced graphene oxide ultrathin nanosheets with vacancy-enhanced kinetics as superior anodes for sodium-ion batteries, *Nano Energy*, 2018, **53**, 524–535.

35 J. Yang, H. Gao, S. Men, Z. Shi, Z. Lin, X. Kang and S. Chen, $CoSe_2$ Nanoparticles Encapsulated by N-Doped Carbon Framework Intertwined with Carbon Nanotubes: High-Performance Dual-Role Anode Materials for Both Li- and Na-Ion Batteries, *Adv. Sci.*, 2018, **5**, 1800763.

36 H. Gao, T. Zhou, Y. Zheng, Q. Zhang, Y. Liu, J. Chen, H. Liu and Z. Guo, CoS Quantum Dot Nanoclusters for High-Energy Potassium-Ion Batteries, *Adv. Funct. Mater.*, 2017, **27**, 1702634.

37 Q. Yu, B. Jiang, J. Hu, C. Y. Lao, Y. Gao, P. Li, Z. Liu, G. Suo, D. He, W. A. Wang and G. Yin, Metallic Octahedral $CoSe_2$ Threaded by N-Doped Carbon Nanotubes: A Flexible Framework for High-Performance Potassium-Ion Batteries, *Adv. Sci.*, 2018, **5**, 1800782.

38 Z. Xia, H. Sun, X. He, Z. Sun, C. Lu, J. Li, Y. Peng, S. Dou, J. Sun and Z. Liu, *In situ* construction of $CoSe_2$@vertical-oriented graphene arrays as self-supporting electrodes for sodium-ion capacitors and electrocatalytic oxygen evolution, *Nano Energy*, 2019, **60**, 385–393.

39 J. Chen, A. Pan, Y. Wang, X. Cao, W. Zhang, X. Kong, Q. Su, J. Lin, G. Cao and S. Liang, Hierarchical mesoporous $MoSe_2$@CoSe/N-doped carbon nanocomposite for sodium ion batteries and hydrogen evolution reaction applications, *Energy Storage Mater.*, 2019, **21**, 97–106.

40 J. Jin, Y. Zheng, L. B. Kong, N. Srikanth, Q. Yan and K. Zhou, Tuning ZnSe/CoSe in MOF-derived N-doped porous carbon/CNTs for high-performance lithium storage, *J. Mater. Chem. A*, 2018, **6**, 15710–15717.

41 H. Yang, R. Xu, Y. Yao, S. Ye, X. Zhou and Y. Yu, Multicore–Shell Bi@N-doped Carbon Nanospheres for High Power Density and Long Cycle Life Sodium- and Potassiu-Ion Anodes, *Adv. Funct. Mater.*, 2019, **29**, 1809195.

42 T. Zhang, J. Wu, Y. Xu, X. Wang, J. Ni, Y. Li and J. W. Niemantsverdriet, Cobalt and cobalt carbide on alumina/NiAl(110) as model catalysts, *Catal. Sci. Technol.*, 2017, **7**, 5893–5899.

